A flexible and intuitive analytic expression for the metallicity-dependent cosmic star formation rate

L. A. C. VAN SON,[1,2,3] S. E. DE MINK,[3,2,1] R. PAKMOR,[3] MARTYNA CHRUŚLIŃSKA,[3] AND ET AL?

[1]*Center for Astrophysics | Harvard & Smithsonian, 60 Garden St., Cambridge, MA 02138, USA*
[2]*Anton Pannekoek Institute of Astronomy and GRAPPA, Science Park 904, University of Amsterdam, 1098XH Amsterdam, The Netherlands*
[3]*Max Planck Institute for Astrophysics, Karl-Schwarzschild-Str. 1, 85748 Garching, Germany*

ABSTRACT

New observational facilities are probing astrophysical transients such as gravitational wave (GW) sources at ever increasing redshifts. To interpret these observation we need to compare them to predictions from stellar population models. These models are very sensitive to the metallicity-dependent star formation rate density ($\mathcal{S}(Z,z)$). Understanding the behaviour of the adopted $\mathcal{S}(Z,z)$ is essential to explain simulation results. In this work, we propose a simple analytical form for $\mathcal{S}(Z,z)$. The novelty of this model lies in a skewed-lognormal distribution of metallicities, that captures the tail of low metallicity star formation at low redshift. Variations of this analytical form can be easily interpreted, because the parameters are intuitively linked to the shape of $\mathcal{S}(Z,z)$. We fit our analytical form to the star-forming gas of the cosmological TNG100 simulations and find that it is able to capture the main behaviour well. As an example application, we investigate the effect of systematic variations in the $\mathcal{S}(Z,z)$ parameters on the predicted mass distribution of locally merging binary black holes (BBH). Our main findings are I) the low mass end is least affected by variations in $\mathcal{S}(Z,z)$, II) the distribution of metallicities at low redshift affects the normalisation of of the BBH merger rate, while III) the redshift evolution of the metallicity distribution affects the high-mass slope of the mass distribution and IV) the shape of the overall star-formation rate has a small impact on the local mass distribution.

1. INTRODUCTION

A myriad of astrophysical phenomena depend critically on the rate of star formation throughout the cosmic history of the Universe. Transient phenomena, including core collapse supernovae, (pulsational) pair-instability supernovae, long gamma-ray bursts and gravitational wave (GW) events are especially sensitive to the metallicity at which star formation occurs at different epochs throughout the Universe. Gravitational astronomy in particular has seen explosive growth in the number of detections in the past decade (Abbott et al. 2018, 2020, 2021a). In order to correctly model and interpret these observations, it is fundamental to know the rate of star formation at different metallicities throughout cosmic history, i.e. the metallicity-dependent star formation rate density $\mathcal{S}(Z,z)$ (see also the recent review by Chruślińska 2022).

Corresponding author: L. van Son
lieke.van.son@cfa.harvard.edu

It is difficult to observationally constrain the shape of $\mathcal{S}(Z,z)$ (see Chruślińska & Nelemans (2019) for an extensive overview and discussion of relevant observational caveats). Even at low redshifts, the low metallicity part of the distribution is poorly constrained (Chruślińska et al. 2021). Nonetheless, several methods exist to estimate the metallicity dependent star-formation rate. The first method combines a mass-metallicity relation (MZ-relation) and a galaxy stellar mass function (GSMF) (see e.g. ?Chruślińska et al. 2019; Broekgaarden et al. 2021a). Another way is to directly extract the metallicity density fraction from cosmological simulations (Mapelli et al. 2017; Briel et al. 2021, e.g.). Alternatively, one can combine an observed star formation rate, SFRD(z), like from Madau & Dickinson (2014) or ?, and convolve this with some belief about the shape of the metallicity density distribution, such as was was done in ?.

In this work we follow the latter approach and propose a flexible analytical model for the $\mathcal{S}(Z,z)$ that can be fit to the output of both cosmological simulations, and observational data constraints where available. The novelty of this model lies in a skewed-lognormal distribution of metallicities, that captures the tail of low metallic-

ity star formation at low redshift. The purpose of this model is to allow for an intuitive interpretation of the effects of the $\mathcal{S}(Z, z)$ on the inferred rates of astrophysical transients. By adopting an analytical, parametrized form for $\mathcal{S}(Z, z)$, the large uncertainties in $\mathcal{S}(Z, z)$ can be systematically explored.

We describe our model for $\mathcal{S}(Z, z)$ in Section 2. We fit our model to to the star-forming gas in the Illustris TNG100 simulation in Section 4 we demonstrate an example application of our model by systematically varying the parameters that determine the shape of $\mathcal{S}(Z, z)$ and investigate their impact on the local distribution of merging BBH masses. We summarise our findings in Section 5.

2. A CONVENIENT ANALYTIC EXPRESSION FOR THE METALLICITY-DEPENDENT STAR FORMATION RATE DENSITY

We assume that the metallicity dependent star formation rate density can be separated into two independent functions (e.g. Langer & Norman 2006),

$$\mathcal{S}(Z, z) = \mathrm{SFRD}(z) \times \frac{\mathrm{dP}}{\mathrm{dZ}}(Z, z). \quad (1)$$

The first term is the star formation rate density, $\mathrm{SFRD}(z)$, that is the amount of mass formed in stars per unit time and per unit comoving volume at each redshift. The second term, $\mathrm{dP/dZ}(Z, z)$, is a probability density function that expresses what fraction of star formation occurs at which metallicity, at each redshift.

2.1. *The metallicity probability density function*

For the probability distribution of metallicities we draw inspiration from the approach by (e.g. **?**) who used a log-normal distribution. Unfortunately, this expression does not capture the asymmetry well that we see in the results of the cosmological simulations, which show an extended tail towards low metallicity combined with a very limited tail towards higher metallicity, when plotted as a function of $\log_{10} Z$. To capture this behavior we adopt a skewed-log-normal distribution instead. This is an extension of the normal distribution that introduces an additional shape parameter, α, that regulates the skewness (first introduced by O'Hagan & Leonard 1976).

The skewed-log-normal distribution of metallicities is defined as:

$$
\begin{aligned}
\frac{\mathrm{dP}}{\mathrm{dZ}}(Z) &= \frac{1}{Z} \times \frac{\mathrm{dP}}{\mathrm{d}\ln Z} \\
&= \frac{1}{Z} \times \underbrace{\frac{2}{\omega} \phi\left(\frac{\ln Z - \xi}{\omega}\right)}_{(1)} \underbrace{\Phi\left(\alpha \frac{\ln Z - \xi}{\omega}\right)}_{(2)}, \quad (2)
\end{aligned}
$$

where (1) is the standard log-normal distribution, ϕ,

$$\phi\left(\frac{\ln Z - \xi}{\omega}\right) \equiv \frac{1}{\sqrt{2\pi}} \exp\left\{-\frac{1}{2}\left(\frac{\ln Z - \xi}{\omega}\right)^2\right\} \quad (3)$$

and (2) is the new term that allows for asymmetry, which is equal to the cumulative of the log-normal distribution, Φ,

$$\Phi\left(\alpha\frac{\ln Z - \xi}{\omega}\right) \equiv \frac{1}{2}\left[1 + \mathrm{erf}\left\{\alpha\frac{\ln Z - \xi}{\omega\sqrt{2}}\right\}\right] \quad (4)$$

This introduces three parameters, α, ω and ξ each of which may depend on redshift. The first parameter, α, is known as the "shape". It affects the skewness of the distribution and thus allows for asymmetries between metallicities that are higher and lower than the mean. The symmetric log-normal distribution is recovered for $\alpha = 0$. The second parameter, ω is known as the "scale". It provides a measure of the spread in metallicities at each redshift. Finally, ξ, is known as the "location", because this parameter plays a role in setting the mean of the distribution at each redshift.

The location and the mean of the metallicity distribution— To obtain a useful expression for the redshift dependence of the "location" $\xi(z)$ we first express the expectation value or mean metallicity at a given redshift

$$\langle Z \rangle = 2 \exp\left(\xi + \frac{\omega^2}{2}\right) \Phi(\beta\,\omega) \quad (5)$$

where β is

$$\beta = \frac{\alpha}{\sqrt{1 + \alpha^2}}. \quad (6)$$

For a more extended derivation of the moments of the skewed-log-normal, see e.g., Wang et al. (2019). For the evolution of the mean metallicity with redshift we follow Langer & Norman (2006) and **?** in assuming that the mean of the probability density function of metallicities evolves with redshift as:

$$\langle Z \rangle \equiv \mu(z) = \mu_0 \cdot 10^{\mu_z \cdot z}, \quad (7)$$

where μ_0 is the mean metallicity at redshift 0, and μ_z determines redshift evolution of the location. Equating this to Equation 5, we get an expression for $\xi(z)$,

$$\xi(z) = \ln\left(\frac{\mu_0 \cdot 10^{\mu_z \cdot z}}{2\,\Phi(\beta\,\omega)}\right) - \frac{\omega^2}{2}. \quad (8)$$

The scale (and variance) of the metallicity distribution— We will also allow the "scale" ω to evolve with redshift in a similar manner,

$$\omega(z) = \omega_0 \cdot 10^{\omega_z \cdot z}. \quad (9)$$

where ω_0 is the width of the metallicity distribution at $z = 0$, and ω_z the redshift evolution of the scale.

Note that the width, $w(z)$ is not the same as the variance. The variance, $\sigma(z)^2$, can be expressed as

$$\sigma(z)^2 = \omega(z)^2 \left(1 - \frac{2\beta^2}{\pi} \right) \qquad (10)$$

Asymmetry of the metallicity distribution: α —We have considered variations where the "skewness" α varies with redshift but we did not find very significant improvements compared to the simpler assumption where α is kept constant.

In summary, Equation 2 becomes:

$$\frac{dP}{dZ}(Z, z) = \frac{2}{\omega(z)Z} \times \phi \left(\frac{\ln Z - \xi(z)}{\omega(z)} \right) \Phi \left(\alpha \frac{\ln Z - \xi(z)}{\omega(z)} \right),$$
$$(11)$$

where $\xi(z)$ and $\omega(z)$ are defined in Equations 8 and 9 respectively and we have assumed α to be constant.

2.2. *The overall cosmic star formation rate density*

For the star formation rate density, we assume the analytical form proposed by Madau & Dickinson (2014),

$$\mathrm{SFRD}(z) = \frac{d^2 M_{\mathrm{SFR}}}{dt dV_c}(z) = a \frac{(1+z)^b}{1 + [(1+z)/c]^d} \qquad (12)$$

in units of $\left[\mathrm{M}_\odot \, \mathrm{yr}^{-1} \, \mathrm{cMpc}^{-3} \right]$. This introduces four parameters; a which sets the overal normalisation and which has the same units as $\mathrm{SFRD}(z)$ and b, c and d which are unitless and which govern the shape of the overal cosmic star formation rate density with redshift.

Lastly, we combine equations 11 and 12 to form a full metallicity specific star formation rate density as described in equation 1.

3. FIT AGAINST COSMOLOGICAL SIMULATION

We fit our new functional form of $\mathcal{S}(Z, z)$ as defined by equations 1, 11 and 12 to the Illustris-TNG cosmological simulations. We fit for the following nine free parameters $\alpha, \mu_0, \mu_z, \omega_0, \omega_z$, which govern the metallicity dependence and a, b, c and d, which set the overall star formation rate.

Below we briefly discuss the Illustris-TNG simulations, and elaborate on our fitting procedure.

3.1. *Illustris-TNG Cosmological simulations*

The IllustrisTNG-project (or TNG in short Springel et al. 2018; Marinacci et al. 2018; Nelson et al. 2018; Pillepich et al. 2018a; Naiman et al. 2018) considers galaxy formation and evolution through large-scale cosmological hydrodynamical simulations. Such simulations provide the tools to study parts of the Universe

that are not easily accessible by observations. In particular of interest for this work, they simulate the high redshift enrichment of galaxies and the tail of low metallicity star formation at low redshift. Different cosmological simulations produce varying $\mathcal{S}(Z, z)$, depending on the adopted assumptions about the creation and distribution of metals.

The models implemented in the publicly available TNG simulations[1] have lead to many successes. For a more extended discussion focused on the processes that govern the creation, distribution and mixing of metals in in the TNG simulations we refer to Pakmor et al. (2022). In short, star formation in the TNG simulations is calibrated against the Kennicutt–Schmidt relation (Schmidt 1959; Kennicutt 1989). The stellar metallicity yields are and updated version of the original Illustris simulations as described in Pillepich et al. (2018b). Star particles deposit metals into the gas through Type Ia and Type II supernovae, as well as through Asymptotic Giant Branch mass loss. The TNG simulations have been shown to match observational constraints on the mass-metallicity relation of galaxies up to $z = 2$ (Torrey et al. 2019), as well as iron abundances (Naiman et al. 2018) and the metallicity gradients within galaxies at low redshift (Hemler et al. 2021). Several studies have already used the TNG simulations to make predictions for astronomical transient sources (e.g. Briel et al. 2021; Bavera et al. 2022). In particular, Briel et al. (2021) show that the $\mathcal{S}(Z, z)$ from the TNG and the EAGLE (Schaye et al. 2015; Crain et al. 2015) simulations provide the best agreement between observed and predicted cosmic rates for electromagnetic and gravitational-wave transients.

On the other hand, large uncertainties and crude approximations remain in all contemporary cosmological simulations, thus also in the TNG simulations. For example, dust is not included in the TNG simulations, which could mean that metallicity of the star-forming gas is overestimated. Furthermore, all mass loss from massive stellar winds (e.g. Dray et al. 2003), pair-pulsational supernovae (e.g. Renzo et al. 2020) binary interactions (e.g. Farmer et al. 2021) and their ionising effects (Götberg et al. 2020; Doughty & Finlator 2021) are ignored. Moreover, the uniform ionising UV background is turned on abruptly at $z = 6$, which crucially impacts the amount of low metallicity star formation at low redshift.

These large uncertainties call for a generalised form of the $\mathcal{S}(Z, z)$ that can be easily updated when new infor-
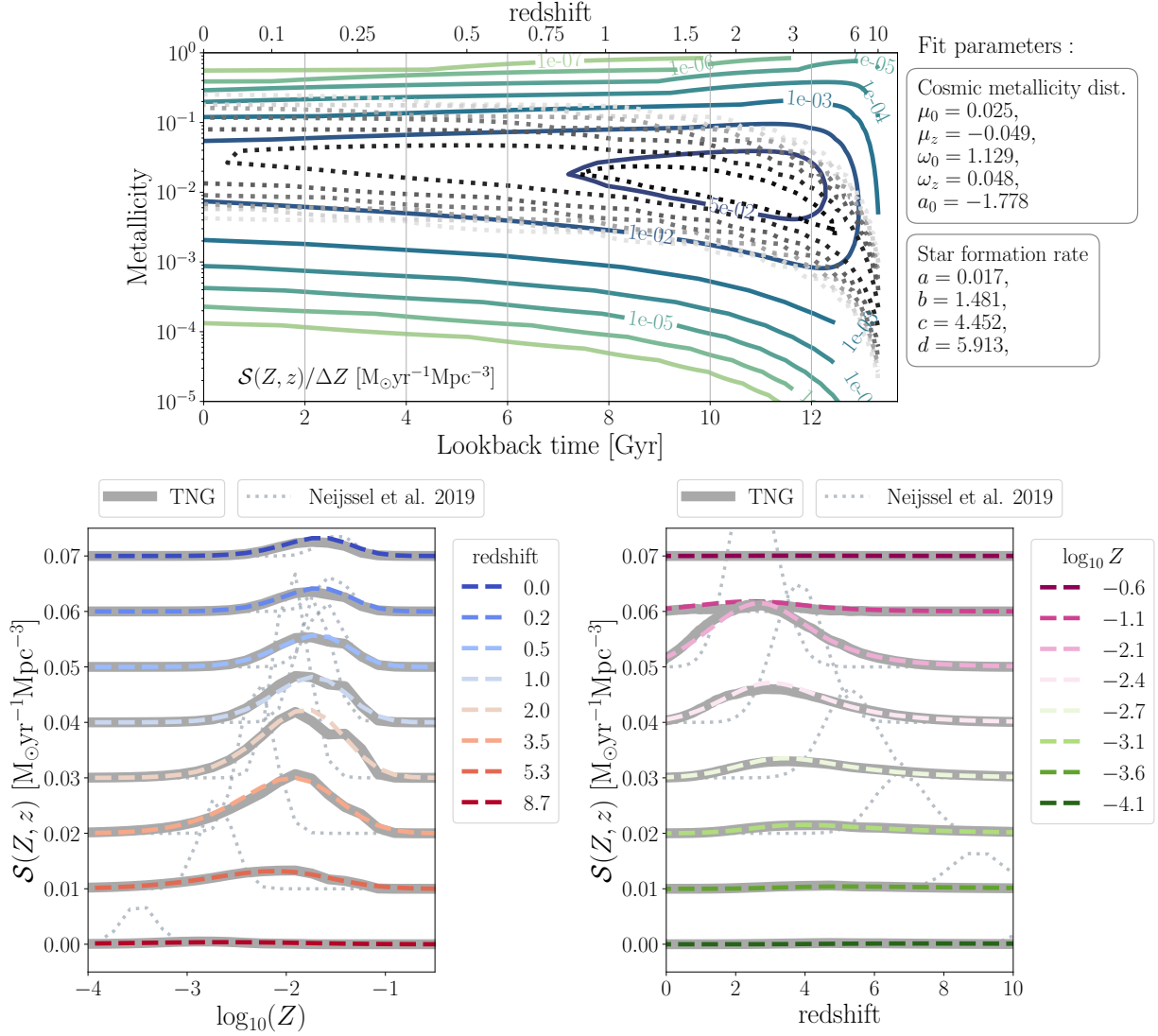
---

[1] https://www.tng-project.org/

Figure 1. Our fiducial $\mathcal{S}(Z,z)$ model, adopting the best fitting parameters (listed on the top right) to fit the TNG100 simulations. The top panel shows the full two dimensional $\mathcal{S}(Z,z)$ linear in time. The bottom left (right) panel shows slices of the distribution in redshift (metallicity). Each slice is displaced by $0.01 \mathrm{M}_\odot \, \mathrm{yr}^{-1} \, \mathrm{Gpc}^{-3}$. We show the TNG100 simulation data with thick gray lines. For comparison, we also show the phenomenological model from **?** in each panel with grey dotted lines. For the latter, the contours in the top panel range from $10^{-7} - 10^{-2} \mathrm{M}_\odot \, \mathrm{yr}^{-1} \, \mathrm{Gpc}^{-3}$. This shows that our analytical model adequately captures the $\mathcal{S}(Z,z)$ of the TNG100 simulations.

mation becomes available, which is the motivation for this work. Although here, we only fit our model to the TNG100 simulation, our prescription can be easily be used to fit other simulated data or observational data of the metallicity dependent star formation rate density [2].

3.2. Choices and binning of the data

We fit equation 1 to the metallicity-dependent star formation rate of the star-forming gas in the TNG100 simulation. For this we use a binned version of the TNG

data $\mathcal{S}(Z,z)_\mathrm{sim}$. We consider metallicities between $Z = -5$ to $\log_{10} Z = 0$ in 30 bins, where we use Z_i to refer to the logarithmic centres of the bins. We ignore star formation in metallicities $\log_{10} Z \leq -5$ as this accounts for less than 1% of the total cosmic star formation rate in these simulations. We consider bins in redshifts between $z = 0$ and $z = 10$, with a step size of $dz = 0.05$, where z_j refers to the centres of the bins.

3.3. Optimisation function

To find a solution we use a method based on the sum of the quadratic differences between the simulations and our fit function. Using a vanilla χ-squared approach

[2] We provide a Jupyter notebook to facilitate this fit here **add link**

does not serve our purposes very well as it does a poor job in fitting regions where the star formation is very low. Using a χ-squared approach on the logarithm of the function instead places far too much weight on trying to fit the star formation rate in regions where the rate is very low or not even significant. After experimenting, we find that the following approach gives us satisfactory results.

We first consider a given redshift z_j. For this redshift we compute the sum of the squared residuals between the cosmological simulation and our fit.

$$\chi^2(z_j) \equiv \sum_{Z_i} \left(\mathcal{S}(Z_i, z_j)_{\text{sim}} - \mathcal{S}(Z_i, z_j)_{\text{fit}}\right)^2 \qquad (13)$$

Here, the variable Z_i runs over all redshift bins. We are particularly interested in properly fitting the low metallicity star formation at high redshifts. At high redshifts, the overall cosmic star formation rate is generally lower. To ensure that our fit procedure gives sufficient weight to the behaviour at all redshifts, we introduce a penalisation factor to somewhat reduce the contribution of redshifts where the peak of cosmic star formation occurs, while increasing the weight where at redshifts where the overall cosmic star formation rate is lower. To achieve this we divide $\chi^2(z_j)$ by the star formation $\sum_{Z_i} \mathcal{S}(Z_i, z_j)$ per redshift bin before adding the contribution of all redshifts. Our final expression for the cost function reads

$$\chi = \sum_{z_j} \frac{\chi^2(z_j)}{\sum_{Z_i} \mathcal{S}(Z_i, z_j)} \qquad (14)$$

To minimize this cost funciton, we use `scipy.optimize.minimize` from SciPy v1.6.3 which implements the quasi-Newton method of Broyden, Fletcher, Goldfarb, and Shanno (BFGS, Nocedal & Wright 2006).

3.4. Resulting $\mathcal{S}(Z, z)$

Our best fitting parameters are listed in Table 1. With these fit parameters, $\chi^2(z_j)$ is smaller than $2 \cdot 10^{-4}$ at any given redshift. We will refer to the $\mathcal{S}(Z, z)$ with the parameters listed in Table 1 as our fiducial model.

In Figure 1 we show our fiducial model at different redshifts and metallicities. For clarity, we also show the overall rate of star formation $\text{SFRD}(z)$ in Figure 2. In general, our analytical model captures the metallicity dependent star formation in the TNG100 simulations well (bottom panels of Figure 1). The skewed-log normal metallicity distribution is able to reproduce the overall behaviour that is observed in TNG100 (bottom left panel, but cf. Pakmor et al. 2022, for an in-depth discussion of low metallicity star formation in the

Table 1. Best fitting parameters for our $\mathcal{S}(Z, z)$ fit to TNG100 data.

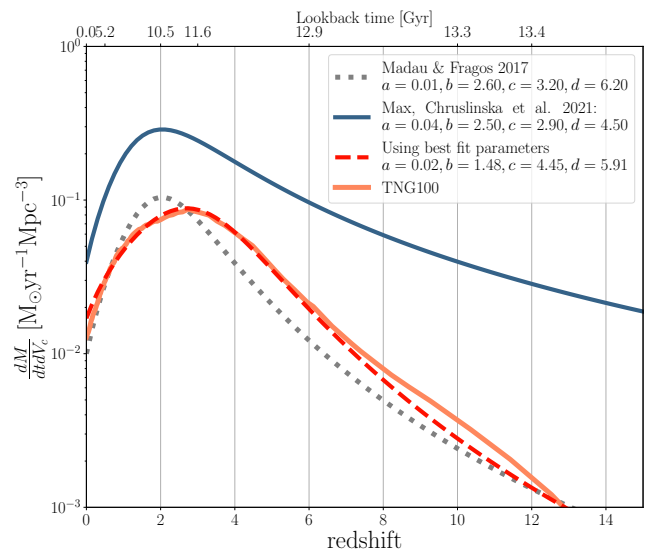| dP/dZ	description	best fit	SFRD(z)	best fit
μ_0	mean metallicity $z = 0$	0.025	a	0.02
μ_z	mean metallicity z evol.	-0.048	b	1.48
α	shape (skewness)	-1.767	c	4.45
ω_0	scale $z = 0$	1.125	d	5.90
ω_z	scale z evol.	0.048		

Figure 2. Comparison of different $\text{SFRD}(z)$

TNG50 simulation). Only minor features like the additional bump just above $\log_{10}(Z) = -2$ at redshift 2 are missed. However, for our purposes, it is more important to prioritise fitting the large scale trends, while we are not so interested in smaller scale fluctuations.

Adopting a skewed-lognormal metallicity distribution allows for a tail of low metallicity star formation out to low redshifts. To emphasise the difference between a skewed-lognormal and a symmetric lognormal distribution, we show the phenomenological model from **?** in dotted grey. Their model falls within the family of functions that is encompassed by our model described in Section 2. [3]

---

[3] The phenomenological model from **?** is recovered by adopting $\mu_0 = 0.035$, $\mu_z = -0.23$, $\omega_0 = 0.39$, $\omega_z = 0$, $\alpha = 0$, $a = 0.01$, $b = 2.77$, $c = 2.9$ and $d = 4.7$.

4. APPLICATION: SYSTEMATIC VARIATIONS OF $\mathcal{S}(Z, z)$ AND THE EFFECT ON THE MASS DISTRIBUTION OF MERGING BBHS

We will now demonstrate the application of our analytical model by systematically varying the parameters in our fiducial $\mathcal{S}(Z, z)$ model, and investigate their effect on the local mass distribution of BBH mergers originating from isolated binaries.

We use the publicly available rapid binary population synthesis simulations presented in van Son et al. (2022). These simulations were run using version v02.19.04 of the open source COMPAS suite (Riley et al. 2022) [4]. COMPAS is based on algorithms that model the evolution of massive binary stars following ??, based on detailed evolutionary models by ?. We refer the reader to the methods section of van Son et al. (2022) for a detailed description of our adopted physics parameters and assumptions. Metallicities of each binary system were sampled from a smooth probability distribution to avoid artificial peaks in the BH mass distribution (e.g. Dominik et al. 2015; Kummer 2020). These simulations provide us with an estimate of the yield of BBH mergers per unit of star-forming mass and metallicity.

We combine the aforementioned yield with a variation of the fiducial $\mathcal{S}(Z, z)$ model described in this work. By integrating over cosmic history, we obtain the local merger rates of BBH systems, which allow us to construct the distribution of source properties at every redshift. The details of this framework are described in van Son et al. (2022), and also in Broekgaarden et al. (2021a) and ?.

We consider variations of each of the parameters that determine the shape of the cosmic metallicity distribution $dP/dZ(Z, z)$ (left two columns of Table 1) and two variations of the SFRD(z), where we keep the metallicity distribution $dP/dZ(Z, z)$ fixed, but vary the overall star-formation rate history SFRD(z) (i.e. all four SFRD(z) parameters at once), to match the values used in ? and Neijssel et al. (2019) respectively (see Figure 2 for reference). To determine the range of parameters that is reasonably allowed by observations, we have compared the $\mathcal{S}(Z, z)$ in the metallicity-redshift plane to the high and low metallicity extreme from Chruślińska et al. (2021) by eye for every variation.

In Figure 5 we show the resulting mass distribution of the more massive component from merging BBHs. We will refer to the more (less) massive component as the primary (secondary) from hereon. In general we note

that the main features in the primary mass distribution remain distinguishable throughout all $\mathcal{S}(Z, z)$ variations.

Changes in the $\mathcal{S}(Z, z)$ have the largest impact on the high mass end of the primary mass distribution, while the impact on the low mass is relatively modest. To quantify this, we annotate the ratio between the maximum and minimum rate at three reference masses; $M_{\mathrm{BH,1}} = 10, 25$, and $40 M_\odot$. At $M_{\mathrm{BH,1}} = 10 M_\odot$, we find that the rate changes by at most a factor 3 for the variations explored in this work. While we find a factor of at most 11 for the change in rate at $M_{\mathrm{BH,1}} = 40 M_\odot$.

Parameter variations that affect shape of $\mathcal{S}(Z, z)$ at low redshift primarily change the normalisation of the mass distribution. See also $\mathcal{R}_{0.2}$, the total BBH merger rate at redshift 0.2, annotated in the legends of Figure 5 ($z = 0.2$ is where the observations are best constrained by the data Abbott et al. 2021b). This is visible for variations that impact the width of the cosmic metallicity distribution at $z = 0$, ω_0, the mean metallicity of the cosmic metallicity distribution at $z = 0$, μ_0, and the skewness of the cosmic metallicity distribution, α (left column of Figure 5). Variations that *increase* the amount of star formation at low metallicity (i.e. for a low mean metallicity $\mu_0 = 0.015$ and a wide metallicity distribution $\omega_0 = 1.4$) increase the predicted BBH merger rate. This is consistent with other work that finds merging BBHs form more efficiently at low metallicities (e.g. Belczynski et al. 2010; ?; Mapelli et al. 2017; Chruślińska et al. 2019; Broekgaarden et al. 2021b).

Although a skewed distribution allows the metallicity distribution to extend to lower values, it simultaniously pushes the expected value of the metallicity distribution to higher values. Hence, the local rate of BBH mergers is lower for the skewed distribution ($\alpha = -3.5$) with respect to the more symmetric variation ($\alpha = -0.9$). However, the total rate of BBH mergers is only changed by about a factor of 2.

Parameters that change the evolution of the metallicity distribution $dP/dZ(Z, z)$ with redshift, such as ω_z and μ_z (top right and centre right panel), primarily affect the slope of the high mass end of the BBH mass distribution. By reducing the amount of low-metallicity star formation at high redshifts, formation channels with long delay times are excluded. In these simulations, the higher mass systems come from the 'stable mass transfer channel' which is characterised by longer delay times (van Son et al. 2022, see also their Figure 6).

Lastly, changing the SFRD(z) has a relatively small effect. **this is in line with findings from (Tang et al. 2020).** We vary the SFRD(z) to match the form described in ? and ? respectively. Both these variations peak at approximately redshift 2. Our fiducial model
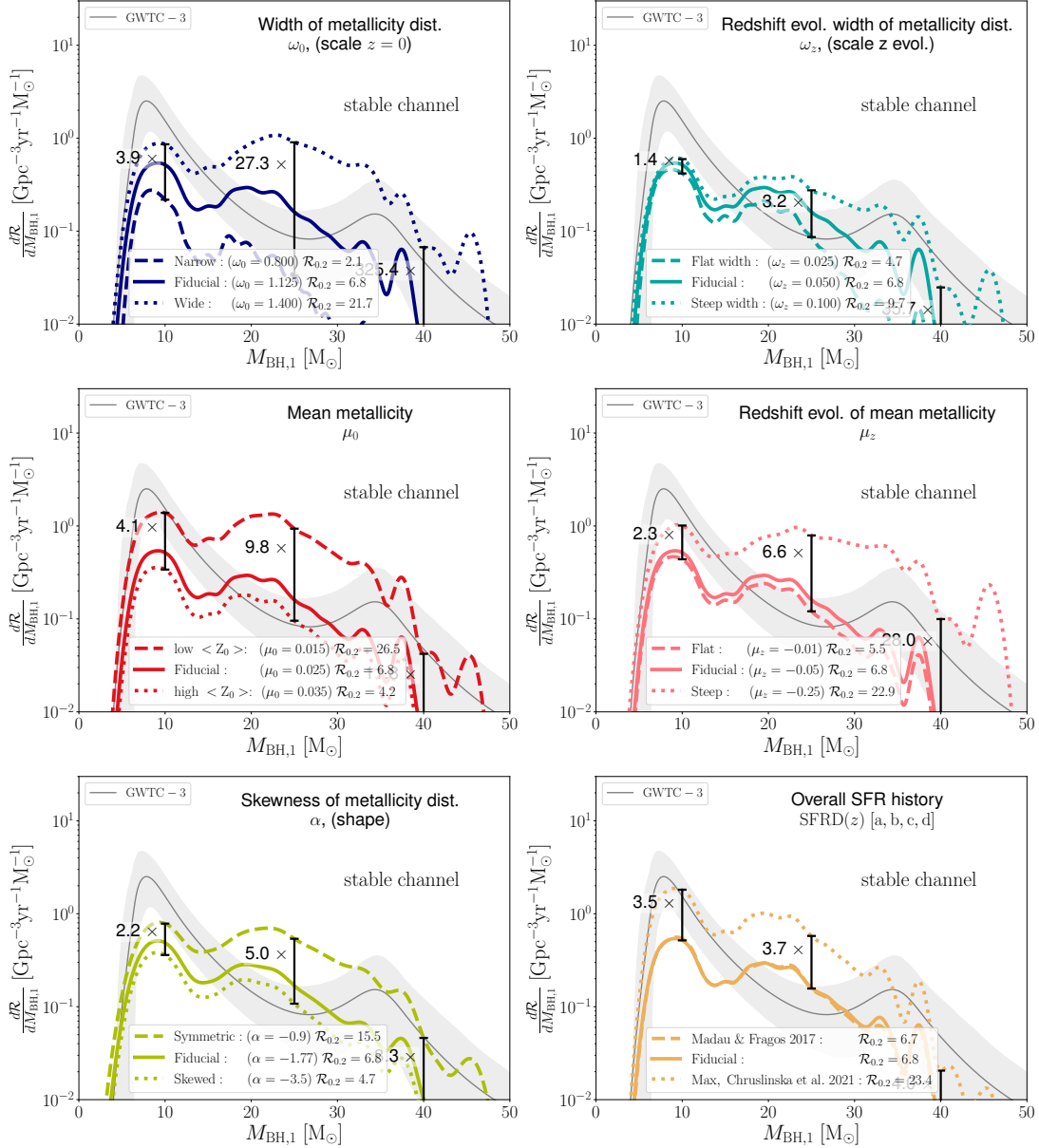
Figure 3. The primary mass distribution of merging BBH systems from the stable mass transfer channel for several variations in $\mathcal{S}(Z, z)$. The first five panels show variations of the cosmic metallicity distribution $dP/dZ(Z, z)$ (eq. 11, parameters listed in the first three columns of Table 1). The bottom right panel shows variations in the magnitude of the star formation rate with redshift, i.e. $SFRD(z)$. For the latter we vary the four fiducial parameters of $SFRD(z)$ simultaneously (last two columns of Table 1). All panels are shown at a reference redshift of $z = 0.2$, with the corresponding predicted BBH merger rate annotated in the legend. We show the power-law + peak model from Abbott et al. (2021b) in grey. Lastly we annotate the relative change in the rate at three reference masses: $10 M_\odot$, $25 M_\odot$ and $40 M_\odot$. Variations in $\mathcal{S}(Z, z)$ have the largest impact on the high mass end of the distribution, while around $M_{BH,1} = 10$, variations are smaller than a factor of 3.

(that follows the $SFRD(z)$ from TNG) peaks at about redshift 2.8. The overall normalisation of **?** is higher than the normalisation of our fiducial model. Regardless of these differences, the rate of BBH mergers at $z = 0.2$ changes no more than 20%, and the shape of the primary mass distribution remains almost constant. We understand this small effect as follows: our fiducial metallicity distribution $dP/dZ(Z, z)$ is almost constant

up to redshift ~ 3. Hence shifting the location of the peak $SFRD(z)$ from 2.8 to 2 has a small effect. Furthermore, even though these models have varying peak values for $SFRD(z)$, the integrated total stellar mass formed is similar between the models.
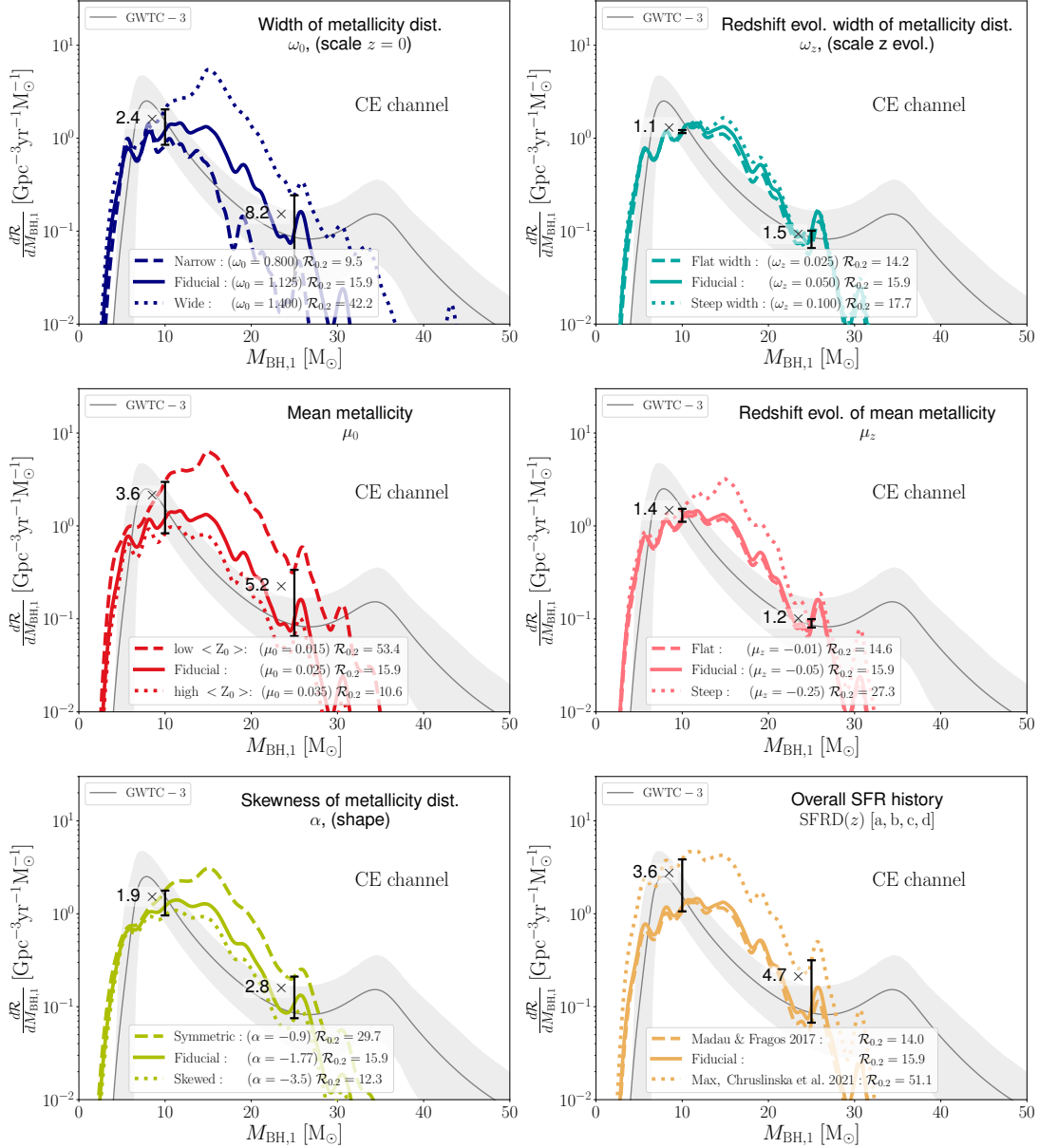
5. DISCUSSION & ? SUMMARY

Figure 4. Same as Figure 5, but for the Common envelope channel.

Chruślińska (2022) Fig. 5 actually shows that the *shape* of the mass distribution is *not at all* impacted that much by the SFRD!!

We present a flexible analytic expression for the metallicity-dependent star formation rate, $\mathcal{S}(Z, z)$ (equations 1, 11 and 12). An analytical expression allows for controlled experiments of the effect of $\mathcal{S}(Z, z)$ on dependent values, such as the rate and mass distribution of merging BBHs. The novelty of the model presented in this work is that it adopts a skewed-lognormal for the distribution of metallicities at every redshift $(\mathrm{dP/dZ}(Z, z))$.

The model can capture the general behaviour of cosmological simulations, such as TNG100—We fit our analytical expression for $\mathcal{S}(Z, z)$ to the star-forming gas in the TNG100 simulation, and provide the best fit parameters in Table 1. We show that our model captures the shape and general behaviour of the cosmological simulations well (Figure 1).

We preform a controlled experiment on the effect of $\mathcal{S}(Z, z)$ on the local distribution of merging BBH—As an example, we apply our model to calculate the local rate and mass distribution of the more massive components from merging BBHs ($M_{\mathrm{BH,1}}$) in Figure 5. We systematically vary all five parameters ($\alpha, \mu_0, \mu_z, \omega_0$ and ω_z) that shape the
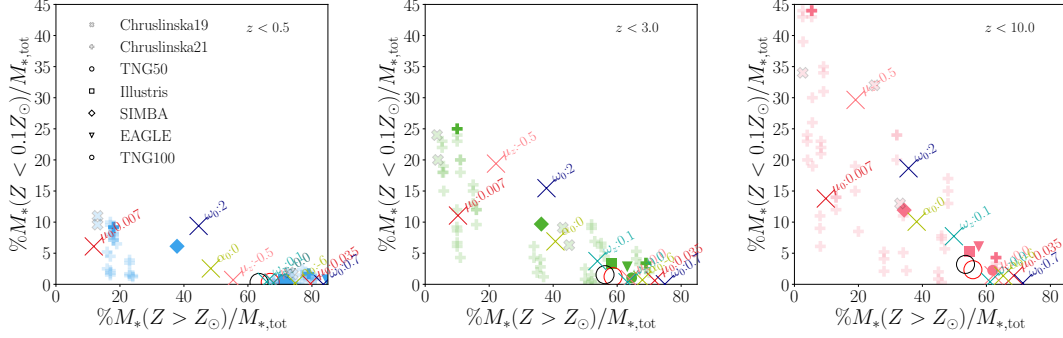
Figure 5. Same as Figure 5, but for the Common envelope channel.

cosmic metallicity distribution $dP/dZ(Z, z)$, and explore two additional variations of the overall star-formation rate $SFRD(z)$, following ? and ? respectively. Our main conclusions are as follows:

- For all variations, the low mass end of the mass distribution is least affected the change in the $\mathcal{S}(Z, z)$.

- The metallicity distribution of star formation at low redshift, primarily impacts the normalisation of the $M_{BH,1}$ distribution (i.e. the total local rate $\mathcal{R}_{0.2}$).

- Parameters that influence the redshift evolution of the metallicity distribution, affect the slope of the high mass end of the $M_{BH,1}$ distribution.

- Changing the overall star-formation history, $SFRD(z)$ has a small effect on the local mass distribution. This is because reasonable variations of the $SFRD(z)$ have a similar value for the total local star-formation rate density, which is relatively well constrained by observations.

The flexibility of the model presented in this work can capture the large uncertainties that remain in the shape and normalisation of the metallicity dependent cosmic star formation history. Our hope is that this expression will provide a useful starting point for making predictions and comparison with observations.

APPENDIX

A. DETERMINING REASONABLE VARIATIONS OF THE $\mathcal{S}(Z, z)$

B. YIELD PER METALLICITY AND MASS

The yield of merging BBH with certain masses, per star forming mass per metallicity

REFERENCES

Abbott, B. P., et al. 2018, Phys. Rev.
https://arxiv.org/abs/1811.12907

Abbott, R., Abbott, T. D., Abraham, S., et al. 2020, arXiv e-prints, arXiv:2010.14527.
https://arxiv.org/abs/2010.14527

Abbott, R., Abbott, T. D., Acernese, F., et al. 2021a, arXiv e-prints, arXiv:2111.03606.
https://arxiv.org/abs/2111.03606

—. 2021b, arXiv e-prints, arXiv:2111.03634.
https://arxiv.org/abs/2111.03634

Bavera, S. S., Fragos, T., Zapartas, E., et al. 2022, A&A, 657, L8, doi: 10.1051/0004-6361/202141979

Belczynski, K., Bulik, T., Fryer, C. L., et al. 2010, ApJ, 714, 1217, doi: 10.1088/0004-637X/714/2/1217

Briel, M. M., Eldridge, J. J., Stanway, E. R., Stevance, H. F., & Chrimes, A. A. 2021, arXiv e-prints, arXiv:2111.08124. https://arxiv.org/abs/2111.08124

Broekgaarden, F. S., Berger, E., Neijssel, C. J., et al. 2021a, arXiv e-prints, arXiv:2103.02608. https://arxiv.org/abs/2103.02608

Broekgaarden, F. S., Berger, E., Stevenson, S., et al. 2021b, arXiv e-prints, arXiv:2112.05763. https://arxiv.org/abs/2112.05763

Chruślińska, M. 2022, arXiv e-prints, arXiv:2206.10622. https://arxiv.org/abs/2206.10622

Chruślińska, M., & Nelemans, G. 2019, MNRAS, 488, 5300, doi: 10.1093/mnras/stz2057

Chruślińska, M., Nelemans, G., & Belczynski, K. 2019, MNRAS, 482, 5012, doi: 10.1093/mnras/sty3087

Chruślińska, M., Nelemans, G., Boco, L., & Lapi, A. 2021, MNRAS, 508, 4994, doi: 10.1093/mnras/stab2690

Crain, R. A., Schaye, J., Bower, R. G., et al. 2015, MNRAS, 450, 1937, doi: 10.1093/mnras/stv725

Dominik, M., Berti, E., O'Shaughnessy, R., et al. 2015, ApJ, 806, 263, doi: 10.1088/0004-637X/806/2/263

Doughty, C., & Finlator, K. 2021, MNRAS, 505, 2207, doi: 10.1093/mnras/stab1448

Dray, L. M., Tout, C. A., Karakas, A. I., & Lattanzio, J. C. 2003, MNRAS, 338, 973, doi: 10.1046/j.1365-8711.2003.06142.x

Farmer, R., Laplace, E., de Mink, S. E., & Justham, S. 2021, ApJ, 923, 214, doi: 10.3847/1538-4357/ac2f44

Götberg, Y., de Mink, S. E., McQuinn, M., et al. 2020, A&A, 634, A134, doi: 10.1051/0004-6361/201936669

Hemler, Z. S., Torrey, P., Qi, J., et al. 2021, MNRAS, 506, 3024, doi: 10.1093/mnras/stab1803

Kennicutt, Robert C., J. 1989, ApJ, 344, 685, doi: 10.1086/167834

Kummer, F. 2020, UvA Scripties

Langer, N., & Norman, C. A. 2006, ApJL, 638, L63, doi: 10.1086/500363

Madau, P., & Dickinson, M. 2014, ARA&A, 52, 415, doi: 10.1146/annurev-astro-081811-125615

Mapelli, M., Giacobbo, N., Ripamonti, E., & Spera, M. 2017, MNRAS, 472, 2422, doi: 10.1093/mnras/stx2123

Marinacci, F., Vogelsberger, M., Pakmor, R., et al. 2018, MNRAS, 480, 5113, doi: 10.1093/mnras/sty2206

Naiman, J. P., Pillepich, A., Springel, V., et al. 2018, MNRAS, 477, 1206, doi: 10.1093/mnras/sty618

Neijssel, C. J., Vigna-Gómez, A., Stevenson, S., et al. 2019, MNRAS, 490, 3740, doi: 10.1093/mnras/stz2840

Nelson, D., Pillepich, A., Springel, V., et al. 2018, MNRAS, 475, 624, doi: 10.1093/mnras/stx3040

Nocedal, J., & Wright, S. 2006, Numerical optimization, 2nd edn., Springer series in operations research and financial engineering (New York, NY: Springer). http://gso.gbv.de/DB=2.1/CMD?ACT=SRCHA&SRT= YOP&IKT=1016&TRM=ppn+502988711&sourceid= fbw_bibsonomy

O'Hagan, A., & Leonard, T. 1976, Biometrika, 63, 201, doi: 10.1093/biomet/63.1.201

Pakmor, R., Simpson, C. M., van de Voort, F., et al. 2022, MNRAS, 512, 3602, doi: 10.1093/mnras/stac717

Pillepich, A., Nelson, D., Hernquist, L., et al. 2018a, MNRAS, 475, 648, doi: 10.1093/mnras/stx3112

Pillepich, A., Springel, V., Nelson, D., et al. 2018b, MNRAS, 473, 4077, doi: 10.1093/mnras/stx2656

Renzo, M., Farmer, R., Justham, S., et al. 2020, A&A, 640, A56, doi: 10.1051/0004-6361/202037710

Riley, J., Agrawal, P., Barrett, J. W., et al. 2022, ApJS, 258, 34, doi: 10.3847/1538-4365/ac416c

Schaye, J., Crain, R. A., Bower, R. G., et al. 2015, MNRAS, 446, 521, doi: 10.1093/mnras/stu2058

Schmidt, M. 1959, ApJ, 129, 243, doi: 10.1086/146614

Springel, V., Pakmor, R., Pillepich, A., et al. 2018, MNRAS, 475, 676, doi: 10.1093/mnras/stx3304

Tang, P. N., Eldridge, J. J., Stanway, E. R., & Bray, J. C. 2020, MNRAS, 493, L6, doi: 10.1093/mnrasl/slz183

Torrey, P., Vogelsberger, M., Marinacci, F., et al. 2019, MNRAS, 484, 5587, doi: 10.1093/mnras/stz243

van Son, L. A. C., de Mink, S. E., Callister, T., et al. 2022, ApJ, 931, 17, doi: 10.3847/1538-4357/ac64a3

Wang, K., Yu, S., & Peng, W. 2019, Journal of Aerosol Science, 134, 95, doi: https://doi.org/10.1016/j.jaerosci.2019.04.013